Original Article

Parametric fluid mechanics study of vessel geometry and blood rheology: Structural absence of a Pareto trade-off

Tulus Tulus[1*], Jonathan L. Marpaung[1], Nuraini A. Aziz[2], Tulus J. Marpaung[3], Suriati Suriati[4], Muhammad R. Syahputra[1] and Putri K. Nasution[1]

[1]Department of Mathematics, Universitas Sumatera Utara, Medan, Indonesia; [2]Department of Mechanical Engineering, Universiti Putra Malaysia, Putrajaya, Malaysia; [3]Statistics Program, Faculty of Vocational Education, Universitas Sumatera Utara, Medan, Indonesia; [4]Department of Information Technology, Universitas Harapan Medan, Medan, Indonesia

*Corresponding author: tulus@usu.ac.id

Abstract

Cardiovascular hemodynamics in narrowed arteries are heavily dictated by local geometry and complex fluid properties, but multi-objective optimization loops using full Navier–Stokes solves remain computationally prohibitive. The aim of this study was to evaluate a multi-objective parametric framework for non-Newtonian blood flow through stenosed arteries and determine whether competing trade-offs exist between geometric narrowing and fluid rheology. The framework combines a Gaussian-parametrized stenosis model with the Carreau–Yasuda rheological law under a reduced-order, lubrication-theory formulation. At each axial position, the model prescribes a parabolic velocity profile scaled by mass conservation, a kinematic approximation that replaces a coupled Navier–Stokes solve. Two separate parametric optimization analyses were conducted with an NSGA-II scheme over three engineering metrics (peak wall shear stress, pressure drop, and viscous energy loss). The first analysis varied stenosis severity and width with rheology fixed, whereas the second varied rheological parameter (μ_0, n, λ) with a severe stenosis fixed. Across four representative configurations, peak velocity and maximum wall shear stress depended on severity alone (0.57 m/s and 1.26 Pa at δ=0.3; 1.00 m/s and 3.80 Pa at δ=0.6), whereas pressure drop and energy loss also rose with stenosis width. Both algorithmic runs converged to a single corner of their mathematical domains rather than a spread Pareto front. Analytical arguments and uniform sampling grids confirmed that each objective changes monotonically with each isolated parameter, causing a single corner solution to dominate each domain. The framework demonstrates the structural behavior of the simplified fluid formulation rather than competing physical optima. An independent, transient 3D COMSOL simulation illustrated a proximal–distal pressure difference varying over the cardiac cycle (peak 3.5 mmHg) to highlight transient physical behaviors omitted by steady-state models. These findings suggest that reduced-order computational formulations structurally govern local fluid indices, demonstrating that geometry and rheology do not present a Pareto trade-off within this kinematic framework.

Keywords: Blood flow simulation, stenosis, non-Newtonian fluid, reduced-order model, hemodynamic optimization

Introduction

Cardiovascular disease remains the leading cause of death worldwide, with more than 17.9 million deaths each year according to the World Health Organization. Atherosclerotic plaque

Copyright: © 2026 by the authors. This is an open access article distributed under the terms and conditions of the CC BY-NC 4.0.

Received: July 29, 2026 - Revised: November 8, 2026 - Accepted: November 14, 2026 - Published online: November 18, 2026

narrows the arterial lumen and disturbs local flow: stenotic segments can carry pressure gradients above 50 mmHg, and wall shear stress (WSS) at the throat can rise to 2.5–3.0 Pa, compared with about 1.0–1.5 Pa in healthy segments. Blood is shear-thinning, so its apparent viscosity falls as the shear rate rises through a constriction. A stenosis positioned near a bifurcation generates persistent vortices and recirculation that favor thrombus formation [1], and comparable disturbances reappear around malapposed stents and across different stent designs [2,3]. Quantifying how stenosis geometry and blood rheology shape WSS and pressure is therefore central to computational studies of arterial disease.

Computational fluid dynamics (CFD) is widely used to analyze flow in stenosed arteries, from patient-specific models combined with 4D-flow MRI [4] to idealized geometries. Non-Newtonian rheology measurably changes the predicted WSS and flow patterns in renal, carotid, and intracranial stenoses [5-7], and an early finite-difference analysis of shear-thinning flow through an axisymmetric stenosis quantified the resulting shift in wall shear stress and pressure relative to Newtonian flow [8]. Finite volume schemes are the usual choice for curved and non-uniform geometries [9,10]. Other studies have extended these models to hematocrit-dependent viscosity in nanofluid blood flow [11], multiple stenoses of varying shape [12], fractional-order rheology [13], wall slip [14], body acceleration with Womersley-type inflow [15], data-assimilated boundary conditions [16], magnetohydrodynamic and bioconvective effects [17-19], viscoelastic blood models [20,21], curved porous walls [22], and nanofluid formulations for drug delivery, thermal therapy and slip flow [23-25]. In each of these studies, either the geometry or the rheology is varied while the other is held fixed, and neither is treated as a search variable.

A separate body of work couples CFD with formal optimization. Genetic algorithms [26] and response-surface methods [27] have been used to tune flow models, but most biomedical applications optimize a manufactured object, such as blood-pump impellers [28,29], an artificial heart pump [30] or cardiovascular stents [31-34], within the wider field of computational cardiac modeling [35]. Stent optimization has progressed from CFD-coupled shape optimization [32] to multi-objective optimization with a Kriging surrogate [33] and topology optimization that weighs structural and hemodynamic parameters together [34]. In all of these studies, the vessel or lesion geometry is fixed, and the device is refined. An earlier work applied the finite volume method to non-Newtonian pulsatile flow in atherosclerotic vessels without an optimization step [36].

None of the aforementioned published studies treats both the stenosis shape (δ, σ) and the non-Newtonian rheology (μ_0, n, λ) as search variables. Thus, this present study addresses that gap with a framework that combines a Gaussian-shaped stenosis, the Carreau–Yasuda rheological law, a reduced-order lubrication-theory flow formulation, and NSGA-II multi-objective searches. Geometry and rheology were explored in two separate searches, each minimizing three numerical outputs: peak WSS, pressure drop, and viscous energy loss. A separate, unmatched transient COMSOL Multiphysics simulation illustrates the pulsatile pressure behavior that the steady model omits. The main contribution of this study is to establish, through analytical and numerical analyses, that within this formulation and these parameter domains, the three outputs do not exhibit trade-offs, so the searches return a single boundary point instead of a spread Pareto front.

Methods

Study design and workflow

The study workflow is presented in **Figure 1**. (i) Model formulation defined the Gaussian stenosis geometry, the Carreau–Yasuda rheology, the boundary conditions, and the reduced-order kinematics; a quadrature-refinement test assessed the accuracy of the numerical integration. (ii) An internal consistency check on a healthy segment (δ=0) confirmed that the implementation reproduces the prescribed Poiseuille profile; this check tested the code, not the physics. (iii) Four representative configurations (Cases A–D), manually specified, were evaluated forward to separate the effects of stenosis severity and width; they were not optimization outputs. (iv) Two separate NSGA-II searches, one over geometry with rheology fixed and one over rheology with geometry fixed, were conducted to minimize the three numerical outputs. (v) An analytical derivation and an exhaustive grid evaluation verified the search outcome over the stated domains.

None of these steps validated the physiological accuracy of the reduced-order model. A separate transient COMSOL simulation, unmatched in geometry, rheology, and boundary conditions, constituted an independent branch that illustrated pulsatile pressure behavior and did not contribute results to steps (i)–(v). The computational steps used to evaluate a single configuration within steps (ii)–(v) are listed in **Table 1**.

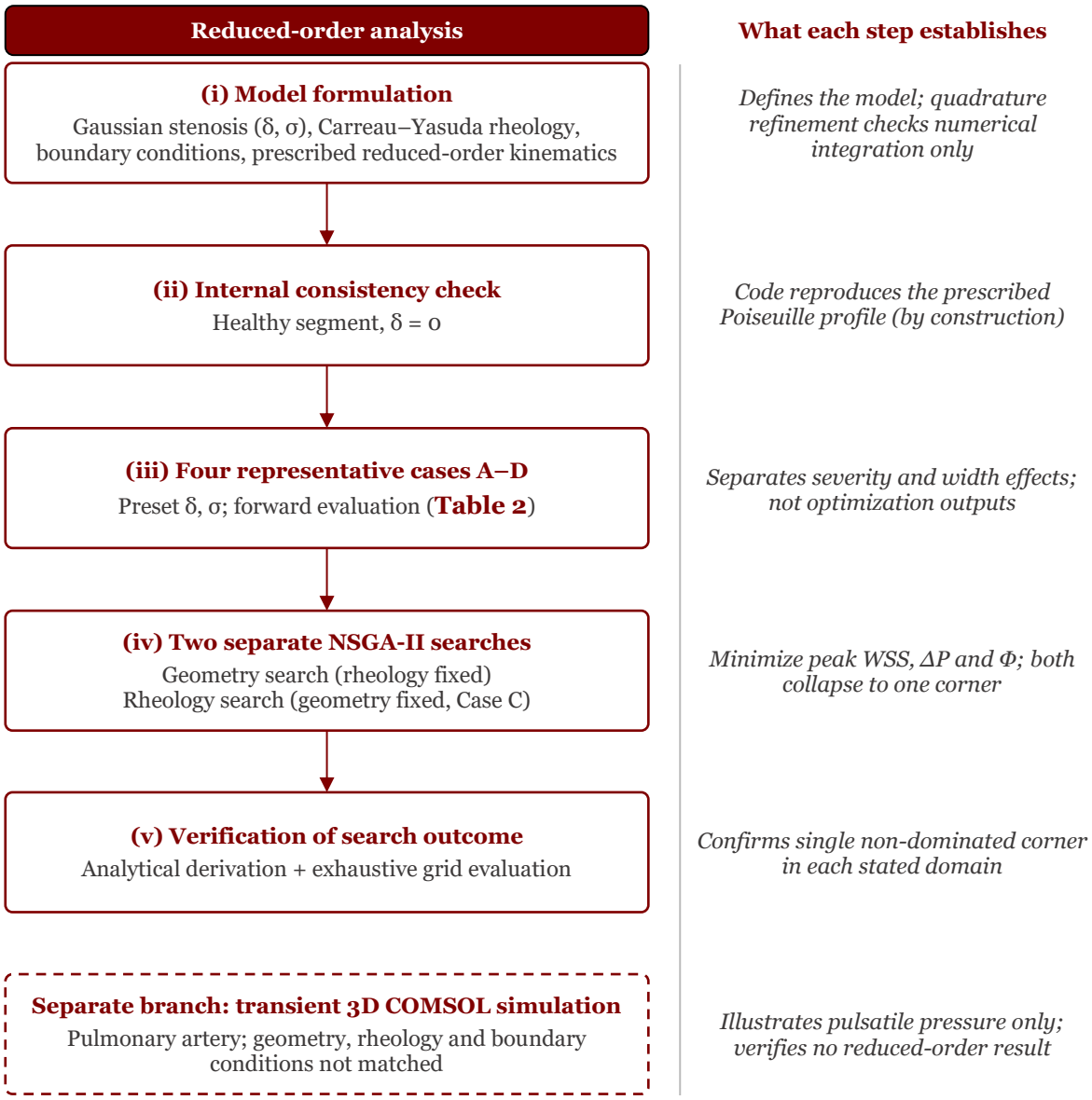

Figure 1. Study workflow. Steps (i)–(v) form the reduced-order analysis; the dashed box marks the separate, unmatched COMSOL simulation, which is illustrative only. The right-hand column states what each step establishes.

Blood flow as a non-Newtonian fluid

In modeling blood flow through stenosed arteries, it is essential to consider the rheological nature of blood. Unlike ideal Newtonian fluids with constant viscosity, blood exhibits non-Newtonian shear-thinning behavior, meaning its apparent viscosity decreases with increasing shear rate. This property is primarily attributed to the deformation and aggregation of red blood cells (RBCs), which dominate blood's mechanical response in microvascular and pathological conditions. To capture this behavior accurately, the Carreau–Yasuda model was employed, providing a smooth transition between the zero-shear viscosity (high viscosity at low shear rates) and the infinite-shear viscosity (low viscosity at high shear rates), which is highly suitable for physiological blood flow simulations. The general form of the Carreau–Yasuda model is given by **Equation 1**.

$$\mu(\dot{\gamma}) = \mu_\infty + (\mu_0 - \mu_\infty)[1 + (\lambda\dot{\gamma})^\alpha]^{\frac{n-1}{\alpha}} \quad (1)$$

Where μ is the apparent viscosity as a function of shear rate; μ0 is the zero-shear viscosity; μ∞ is the infinite-shear viscosity; λ is the time constant (relaxation parameter); n is the power-law index (with n<1 indicating shear-thinning behavior); and α is a fitting parameter controlling the sharpness of transition between low- and high-shear regions. The shear rate is typically defined by **Equation 2**.

$$\dot{\gamma} = \sqrt{2D:D} = \sqrt{2\sum_{i,j}\left(\frac{\partial u_i}{\partial x_j} + \frac{\partial u_j}{\partial x_i}\right)^2} \quad (2)$$

Where D is the strain-rate tensor and u_i are the components of the velocity field. In the context of blood flow within large arteries such as the carotid or coronary arteries, it is valid to model the flow as incompressible, laminar, and steady or pulsatile under certain conditions. The governing equations that describe such flow are the incompressible Navier–Stokes equations, which represent the conservation of mass (**Equation 3**) and momentum (**Equation 4**).

$$\nabla . u = 0 \quad (3)$$

$$\rho\left(\frac{\partial u}{\partial t} + u.\nabla u\right) = -\nabla p + \nabla.[\mu(\dot{\gamma})(\nabla u) + (\nabla u)^T] \quad (4)$$

Where u is the velocity vector; p is the pressure field; ρ is the blood density; μ(γ̇) is the shear-dependent viscosity from the Carreau-Yasuda model; ∇u is the velocity gradient tensor; and t is time. **Equations 3** and **4** are the parent governing equations of this study. In a full solution, μ(γ̇) enters the momentum equation and the velocity field adjusts to the local viscosity. The present study does not solve this coupled system. The reduced-order model described below prescribes the velocity profile from geometry and mass conservation and then evaluates the Carreau–Yasuda viscosity on the resulting shear-rate field, so viscosity never feeds back on velocity. Only the separate COMSOL simulation described below solves the full governing equations using a different geometry.

Arterial geometry modeling (Gaussian-shaped stenosis)

The geometry of a stenosed artery plays a crucial role in determining the local hemodynamic environment, particularly in modulating flow acceleration, pressure drop, and WSS. In this study, a two-dimensional (2D) planar (channel-type) simplified model of a straight arterial segment with a single, symmetric stenosis is constructed to analyze the impact of geometrical narrowing on blood flow behavior. The geometry is defined parametrically using a Gaussian function, which allows for smooth, differentiable variation in the lumen radius and offers control over key parameters such as the degree and width of stenosis. Let R0 denote the nominal (healthy) radius of the artery, and let R(x) represent the radius of the arterial wall along the axial direction x. The Gaussian profile of the stenosis is given by **Equation 5**.

$$R(x) = R_0\left(1 - \delta.exp\left(-\frac{(x - x_s)^2}{2\sigma^2}\right)\right) \quad (5)$$

Where R(x) is the radius of the artery at position x (in m); δ is the maximum relative degree of stenosis (dimensionless, 0<δ<1); x0 is the center position of the stenosis along the axial length; σ is the Gaussian width parameter that determines how localized or spread the stenosis is; and R0 is the healthy artery radius before the stenosis (R0=5 mm in all simulations reported here). This Gaussian formulation creates a smooth, symmetric narrowing of the artery, avoiding sharp gradients that could introduce numerical instability into an iterative discretization scheme, while also keeping the reduced-order model used in this study well-behaved. By varying the parameters δ and σ, different clinical severity levels and geometrical shapes of stenoses can be simulated; small values of σ result in narrow, localized stenoses, while larger values lead to more gradual narrowing.

The stenosis geometry was defined using a Gaussian profile. The segment length (80 mm) is eight times the healthy lumen width, which places the stenosis well away from the inlet and outlet.

Gaussian stenosis profiles of this kind are widely used in idealized studies [15,36]. In the geometric search, δ and σ are the search variables; apart from the search bounds stated below, no physiological constraint is imposed on them.

Boundary conditions and physiological assumptions

The reduced-order model uses four conditions. At the inlet, the healthy-segment velocity profile is the steady planar-Poiseuille parabola of **Equation 6** with centerline velocity u_in=0.4 m/s, which fixes the flow rate Q0 for the whole segment.

$$u(y) = u\left(1 - \left(\frac{y}{R(x)}\right)^2\right)_{max} \quad (6)$$

Where u(y) is the axial velocity as a function of the transverse distance (y) from the centerline (the coordinate y of the planar model); u_max is the centerline velocity; and R(x) is the local artery radius. Based on the inlet mean velocity (2u_in/3), the healthy lumen width 2R0, and the inlet wall viscosity, the inlet Reynolds number is about 720. The reduced-order formulation neglects convective inertia, which is one of its approximations (see Discussion). At the outlet, the gauge pressure is set to zero (**Equation 7**), which fixes the reference level of the pressure field p(x).

$$p = 0 \quad (7)$$

The wall is rigid and no-slip (**Equation 8**), and the prescribed profile vanishes at y = ±R(x), so it satisfies **Equation 8** by construction. It is also symmetric about the centerline and therefore satisfies the symmetry condition in **Equation 9** (zero normal velocity and zero shear stress at y=0). Wall deformation and fluid–structure interaction are neglected.

$$u_{wall} = 0 \quad (8)$$

$$\frac{\partial u}{\partial y} = 0, \quad v = 0 \quad \text{at symmetry line} \quad (9)$$

The model uses the following baseline blood properties: density (ρ) 1060 kg/m³; zero-shear viscosity (μ0) 0.0050 Pa·s; infinite-shear viscosity (μ∞) 0.0035 Pa·s; power-law index (n) 0.8; time constant (λ) 3.313 seconds; and transition parameter (α) 2. The values of λ and α follow the widely used Cho–Kensey parameterization, while μ0 and n define a mildly shear-thinning baseline; the rheology search described below extends μ0, n, and λ to published healthy-blood values [37]. For interpretation only, the results are compared with a literature-cited WSS range of approximately 1–7 Pa and an upper physiological pressure of approximately 200 mmHg (26.7 kPa). These are reporting benchmarks, not constraints: the searches described below minimize the three numerical outputs without any physiological target, and no configuration is excluded for falling outside these values. Throat WSS was also compared descriptively with the ~1.0–1.5 Pa typical of healthy arterial segments.

Reduced-order hemodynamic model and numerical implementation

To implement the mathematical model described in the previous sections in a form that is tractable for repeated evaluation within a genetic-algorithm search, this study used a reduced-order, lubrication-theory formulation rather than an iterative finite-volume Navier–Stokes solve. At each axial position x, the velocity profile was prescribed directly from the local radius R(x) as the parabolic (planar-Poiseuille) form given in **Equation 6**. This profile is the exact fully developed solution only for a Newtonian fluid; for the shear-thinning Carreau–Yasuda fluid it serves as a prescribed reduced-order kinematic approximation, with the constitutive law applied subsequently to the resulting shear-rate field. The centerline velocity u_max(x) was set by mass conservation from the healthy-artery inlet flow rate, $u_{\max(x)} = \frac{3Q0}{(4R(x))}$, where Q0 = (4/3)u_in R0 is the flow rate per unit depth for an inlet centerline velocity u_in=0.4 m/s. The magnitude of the wall shear rate was obtained from the derivative of the prescribed profile, $\frac{du}{dy}|wall = \frac{2u_{\max(x)}}{R(x)}$), rather than from finite differences on a grid. The Carreau–Yasuda viscosity (**Equation 1**),

evaluated at this wall shear rate $\dot{\gamma}_w$ provided the local WSS, $\tau_w = \mu(\dot{\gamma}_w) \cdot \dot{\gamma}_w$, and, used as a representative cross-sectional viscosity, the local pressure gradient from the planar-Poiseuille relation, $\frac{dp}{dx} = \frac{2\mu(\dot{\gamma})u_{\max(x)}}{R(x)^2}$. The formulation sets local WSS and pressure gradient from geometry and shear-dependent viscosity at every axial station, but it solves no coupled momentum–pressure system, so the velocity field cannot respond to changes in viscosity; the Discussion returns to this property. Peak velocity and maximum WSS occur at the throat, where $R=R_{min}=R_0(1-\delta)$, and are evaluated there in closed form: $u_{max}=3Q_0/[4R_0(1-\delta)]$ and $\tau_{w,max}=\mu(\dot{\gamma}_t)\cdot\dot{\gamma}_t$, where $\dot{\gamma}_t=2u_{max}/[R_0(1-\delta)]$ is the wall shear rate at the throat. Neither expression contains σ. The total pressure drop ΔP was calculated by the integral of $-dp/dx$ along x, and the viscous energy loss is the dissipation rate per unit depth, $\Phi=\int\int \mu(\dot{\gamma})\dot{\gamma}^2\, dy\, dx$ (W/m), with the pointwise shear rate $\dot{\gamma}=2u_{max}|y|/R^2$. Both integrals were evaluated using the trapezoidal rule on 8,001 axial stations, with 64-point Gauss–Legendre quadrature across the lumen for Φ; doubling both resolutions changed ΔP and Φ by less than one part in 10^6, indicating the accuracy of the numerical integration only. As an internal consistency check, Φ was compared with the product $Q_0\Delta P$, which it equals exactly for a Newtonian fluid, to within 0.8% for Cases A–D. The computational steps used to evaluate one configuration are presented in **Table 1**.

An unconstricted configuration (δ=0) was evaluated as an internal consistency check. Because the velocity profile is prescribed, agreement with the Poiseuille profile holds by construction; the check confirms the implementation only and involves no mesh, iteration, or convergence criterion. Four representative configurations were then manually specified to separate the effects of severity and width: Case A (δ=0.3, σ=0.005 m), Case B (δ=0.3, σ=0.015 m), Case C (δ=0.6, σ=0.005 m) and Case D (δ=0.6, σ=0.015 m). A further representative stenosis (δ=0.5, σ=0.01 m) was used to illustrate the axial fields.

Table 1. Computational steps used to evaluate one stenosis configuration in the reduced-order model

Step	Procedure
Inputs	Geometry: R_0=5 mm, L=80 mm, x_0=40 mm, stenosis parameters (δ, σ). Rheology: μ_0, μ_∞, λ, n, α (**Equation 1**). Inlet centerline velocity u_{in}=0.4 m/s, giving $Q_0=(4/3)u_{in}R_0$ per unit depth. Outlet gauge pressure 0 Pa.
1. Axial discretization	Place N=8,001 uniformly spaced stations on $0\le x\le L$ and evaluate R(x) from **Equation 5**. No mesh, control volumes or iteration are involved.
2. Kinematics (prescribed)	$u_{max}(x)=3Q_0/[4R(x)]$ from mass conservation; $U(x,y)=u_{max}(x)[1-(y/R(x))^2]$. The profile is imposed, not solved for.
3. Shear rate	$\dot{\gamma}(x,y)=2u_{max}(x)\|y\|/R(x)^2$; wall value $\dot{\gamma}_w(x)=2u_{max}(x)/R(x)$.
4. Viscosity	$\mu(\dot{\gamma})$ from the Carreau–Yasuda law (**Equation 1**), evaluated at $\dot{\gamma}_w$ for steps 5–6 and at $\dot{\gamma}(x,y)$ for step 7.
5. Wall shear stress	$\tau_w(x)=\mu(\dot{\gamma}_w)\dot{\gamma}_w$; $\tau_{w,max}$ at the throat, $R=R_0(1-\delta)$, in closed form.
6. Pressure	$-dp/dx=2\mu(\dot{\gamma}_w)u_{max}/R^2$; $\Delta P=\int_0^L(-dp/dx)dx$ (trapezoidal rule); $p(x)=\Delta P-\int_0^x(-dp/dx)dx$, so $p(L)=0$.
7. Energy loss	$\Phi=\int_0^L\int \mu(\dot{\gamma})\dot{\gamma}^2\, dy\, dx$ over $-R\le y\le R$ (W/m per unit depth); 64-point Gauss–Legendre quadrature in y, trapezoidal rule in x.
8. Outputs	Peak velocity u_{max} at the throat, $\tau_{w,max}$, ΔP and Φ (presented in **Table 2**); fields U, p and τ_w (presented in **Figures 2** and **4**). Each station is evaluated once, so no residual or convergence criterion applies.

Multi-objective search model

The searches were configured to minimize three numerical outputs of the reduced-order model: the maximum wall shear stress (WSS_{max}), the pressure drop (ΔP), and the viscous energy loss (Φ). Minimizing these outputs is not equivalent to minimizing biological or clinical risk, because both low and high WSS can be unfavorable, and the searches impose no physiological target; any optimum they return is conditional on the chosen objectives and bounds. Two design vectors were searched separately, each isolating one source of variation: a geometric vector $x_{geom}=[\delta, \sigma]$, with δ the maximum degree of stenosis (dimensionless, $0<\delta<1$) and σ the Gaussian width parameter (m), with rheology held at the baseline values above; and a rheological vector $x_{rheo}=[\mu_0, n, \lambda]$, with μ_0 the zero-shear viscosity (Pa·s), n the shear-thinning index and λ the time constant (s), with geometry held at the severe stenosis of Case C (δ=0.6, σ=0.005 m).

Because the two vectors were never varied simultaneously, the study did not perform joint geometry–rheology optimization.

NSGA-II was implemented as Pareto-dominance ranking directly on the unweighted objective vector (fast non-dominated sorting [38], with elitist retention of up to 10 first-front individuals per generation and the remaining population regenerated by Gaussian mutation of randomly chosen first-front members; no crossover or tournament selection was used). Each search ran for 20 generations with a population of 50 and a fixed random seed (42), over the three objectives above (WSS_max, ΔP, energy loss) for the relevant design vector (x_{geom} or x_{rheo}).

The geometry search sampled δ ∈ [0.20, 0.70] and σ ∈ [0.003, 0.020] m, with mutation standard deviations of 0.01 and 0.001 m. The rheology search sampled μ0 ∈ [0.005, 0.056] Pa·s, n ∈ [0.3568, 0.80] and λ ∈ [3.313, 39.418] s, with μ∞=0.0035 Pa·s and α=2 fixed, and mutation standard deviations of 0.001 Pa·s, 0.01 and 0.7 s. These rheological ranges spanned the baseline values described above and the healthy-blood Carreau parameter sets compiled in a published carotid-flow study [37]. The parameter bounds maintained μ0>μ∞, consistent with shear-thinning behavior. Initial populations were drawn uniformly within the bounds, and any mutated value outside a bound was clipped to that bound. Objectives were evaluated with the closed-form throat values and the quadrature described above.

Verification of the search outcome

The search outcome was assessed in three ways. First, the direction in which each objective changes with each parameter, holding the others fixed, was derived analytically from **Equations 1** and **5** and the reduced-order relations above, as described in the next paragraph. Second, all three objectives were evaluated exhaustively on a uniform 26×26 grid over the geometric domain and an 11×11×11 grid over the rheological domain; at each grid point the signs of the differences along each coordinate were recorded, and the non-dominated subset of the grid was extracted by pairwise comparison. Third, Pearson correlations between each parameter and each objective were computed on 500 points drawn uniformly from each domain (seed 42). The derivation applied to the continuous parameter domains, whereas the grid and correlation results were limited to the sampled points.

Each objective is a positively weighted integral of the viscosity on a shear-rate field fixed by geometry: WSS_max=μ(γ̇_t) · γ̇_t at the throat, ΔP=∫(2u_max/R²)μ(γ̇_w)dx and Φ=∫∫γ̇²μ(γ̇)dy dx. Neither the weights nor the shear rates depend on rheology. For rheology, **Equation 1** gives ∂μ/∂μ0=F>0, ∂μ/∂n=(μ0−μ∞)F ln(1+X)/a>0 and ∂μ/∂λ=(μ0−μ∞)(n−1)FX/[λ(1+X)]<0, with X=(λγ̇)^a and F=(1+X)^((n−1)/a), at every shear rate whenever μ0>μ∞ and n<1. For geometry, the throat values depend only on R_min=R0(1−δ), and τ=μ(γ̇) · γ̇ increases with γ̇ for n>0; the integrands of ΔP and Φ increase as the local radius decreases, and R(x) decreases with δ at every x and with σ at every x≠x0. Within a box-shaped domain, if moving from one corner toward any other point, one coordinate at a time, raises or leaves unchanged every objective, that corner dominates all other points and is therefore the only non-dominated point. The argument covers the continuous domain; it does not order pairs of non-corner points, whose objectives can move in opposite directions when several parameters change simultaneously.

Separate transient COMSOL simulation

A transient three-dimensional simulation was performed using COMSOL Multiphysics 6.3 (Polymer Flow Module), based on the vendor's application-library model of blood flow in a stenosed pulmonary artery [39]. The simulation differed from the reduced-order model in geometry, rheology, stenosis representation, and boundary conditions. Its domain comprised a branching pulmonary artery; the stenosis was represented as a porous Brinkman region (permeability 1×10^{-7} m²); and blood was modeled using the Carreau model (μ0=0.056 Pa·s, μ∞=0.00345 Pa·s, λ=3.313 s, n=0.3568, ρ=1120 kg/m³). A periodic inflow velocity with a period of 0.8 s drove the flow; the outlets were held at zero static pressure with backflow suppressed, and the walls were rigid and no-slip. The mesh comprised 89,894 elements, and the solution was stored every 0.02 s up to t=2.4 s (three cycles). Pressure was averaged over one cross-section upstream and one downstream of the stenosis. Neither the four representative cases nor the search optima were evaluated using this model, so it served only to illustrate pulsatile behavior.

Results

Unconstricted control configuration

For the unconstricted configuration (δ=0; **Figure 2A**), the centerline velocity remained constant at 0.40 m/s over the 80 mm segment, with a wall shear rate of 160 s^{-1}, an apparent wall viscosity of 3.93 mPa·s, a uniform WSS of 0.63 Pa, and a pressure drop of 10.1 Pa, as presented in **Figures 2C**, **2E**, and **2F** (dashed lines). The velocity profile at every axial station coincided with the prescribed Poiseuille parabola.

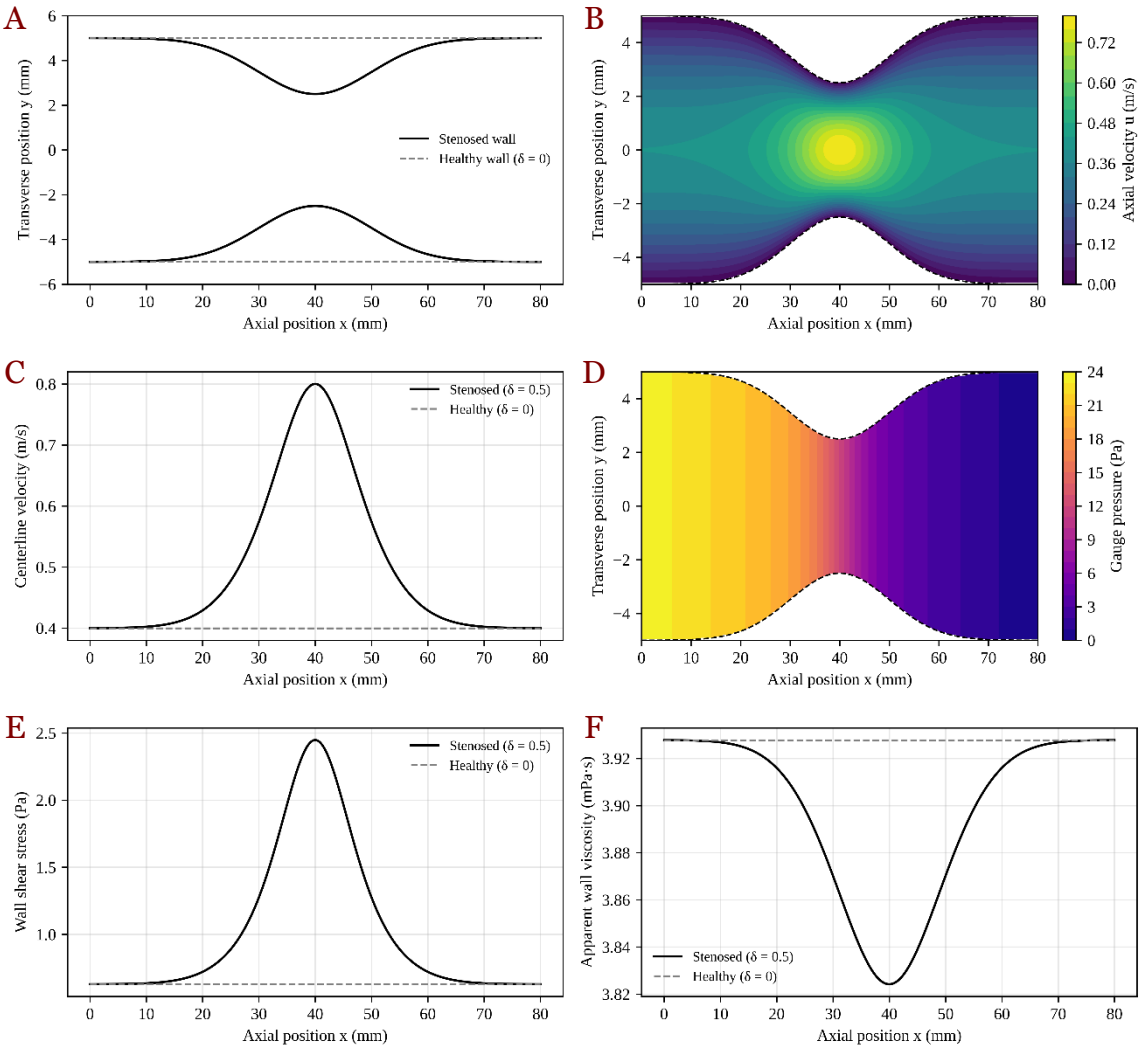

Figure 2. Reduced-order fields for the representative stenosis (δ=0.5, σ=0.01 m; solid lines) and the unconstricted configuration (δ=0; dashed lines). (A) Gaussian stenosis geometry; (B) axial velocity field; (C) centerline velocity; (D) pressure field with the outlet at 0 Pa; (E) wall shear stress; and (F) apparent wall viscosity.

Representative stenosis (δ=0.5, σ=0.01 m)

For the representative stenosis, the centerline velocity increased from 0.40 m/s at the inlet (x=0 mm) to 0.80 m/s at the throat (x=40 mm) and returned to 0.40 m/s at the outlet (x=80 mm), as presented in **Figures 2B** and **2C**. The wall shear rate at the throat reached 640 s^{-1}, and the apparent wall viscosity decreased from 3.93 mPa·s at the inlet to 3.82 mPa·s at the throat, as presented in **Figure 2F**.

The WSS increased from 0.63 Pa at the inlet to a single peak of 2.45 Pa at the throat (x=40 mm) and decreased symmetrically to 0.63 Pa at the outlet; it exceeded 1.0 Pa between x=26.9 and 53.1 mm, as presented in **Figure 2E**. The gauge pressure decreased monotonically from 23.8 Pa at the inlet to 0 Pa at the outlet, with the largest axial gradient at the throat, as presented in **Figure 2D**.

Stenosis severity and width (Cases A–D)

The wall profiles of the four configurations are presented in **Figure 3**. The minimum radius was 3.5 mm for Cases A and B (δ=0.3) and 2.0 mm for Cases C and D (δ=0.6), located at x=40 mm in all cases. The narrowing extended over a longer axial segment in Cases B and D (σ=0.015 m) than in Cases A and C (σ=0.005 m).

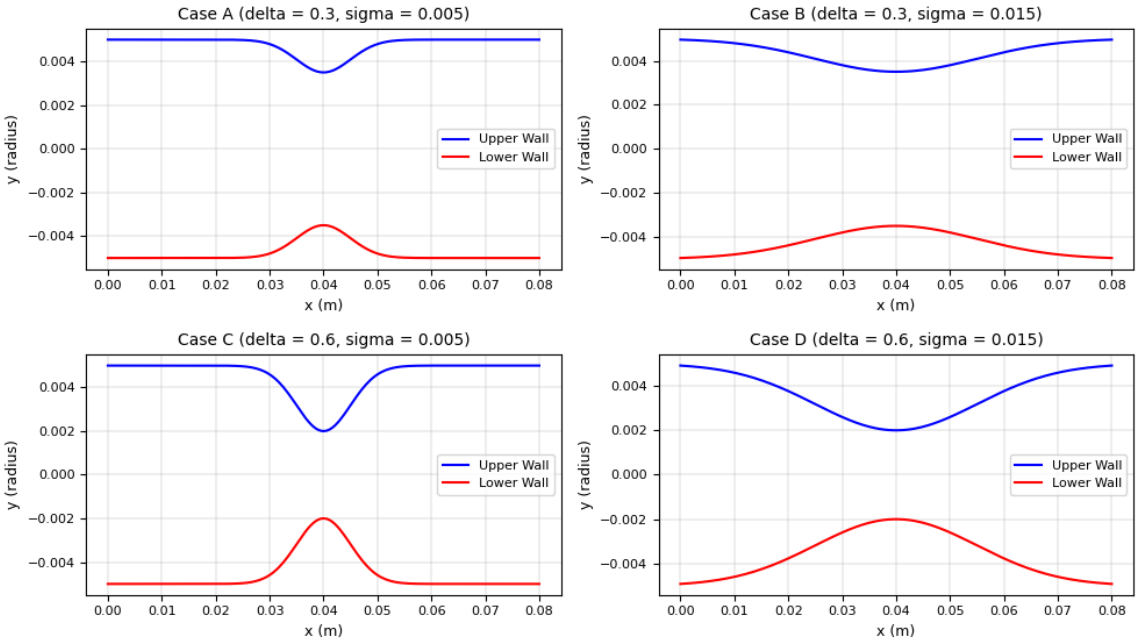

Figure 3. Wall profiles for the four stenosis configurations (Cases A–D).

The hemodynamic quantities of the four configurations are presented in **Table 2**. Cases A and B had the same peak velocity (0.571 m/s) and maximum WSS (1.26 Pa), and Cases C and D had the same peak velocity (1.000 m/s) and maximum WSS (3.80 Pa). At δ=0.3, the pressure drop was 12.4 Pa for σ=0.005 m (Case A) and 17.1 Pa for σ=0.015 m (Case B); at δ=0.6, it was 22.3 Pa (Case C) and 46.7 Pa (Case D). Energy loss followed the same order, from 0.033 W/m (Case A) to 0.125 W/m (Case D).

Table 2. Quantitative hemodynamic characteristics for the four simulated stenosis configurations (reduced-order model)

Case	δ	σ (m)	Peak velocity (m/s)	Max WSS (Pa)	Pressure drop (Pa)	Energy loss (W/m)
A	0.3	0.005	0.571	1.264	12.4	0.0334
B	0.3	0.015	0.571	1.264	17.1	0.0460
C	0.6	0.005	1.000	3.797	22.3	0.0599
D	0.6	0.015	1.000	3.797	46.7	0.1254

σ: Gaussian width parameter; δ: maximum degree of stenosis; Φ: viscous energy loss per unit depth; WSS: wall shear stress

Peak velocity and maximum WSS are closed-form values at the throat; pressure drop and energy loss (viscous dissipation per unit depth) are converged integrals.

The velocity fields and WSS distributions of the four configurations are presented in **Figure 4**. Cases C and D reached the highest centerline velocity (1.00 m/s) and WSS (3.80 Pa) at x=40 mm, and Cases A and B reached 0.57 m/s and 1.26 Pa. The WSS exceeded 1.0 Pa over 14.4 mm of the segment in Case C (x=32.8–47.2 mm) and over 43.4 mm in Case D (x=18.3–61.7 mm); in Cases A and B, the corresponding lengths were 8.4 mm and 25.2 mm.

Multi-objective search outcomes

The outcomes of the two NSGA-II searches and the grid evaluation are presented in **Table 3**. In the geometry search, every first-front member at generation 20 was located at δ=0.20 and σ=0.003 m, with WSS_max=0.97 Pa, ΔP=10.8 Pa, and Φ=0.029 W/m. In the rheology search, every first-front member at generation 20 was located at μ_0=0.005 Pa·s, n=0.3568, and λ=39.418 s, with WSS_max=3.50 Pa, ΔP=20.2 Pa, and Φ=0.054 W/m. Both points were located at the

corners of their respective search domains, and neither search returned a spread front of mutually non-dominated solutions.

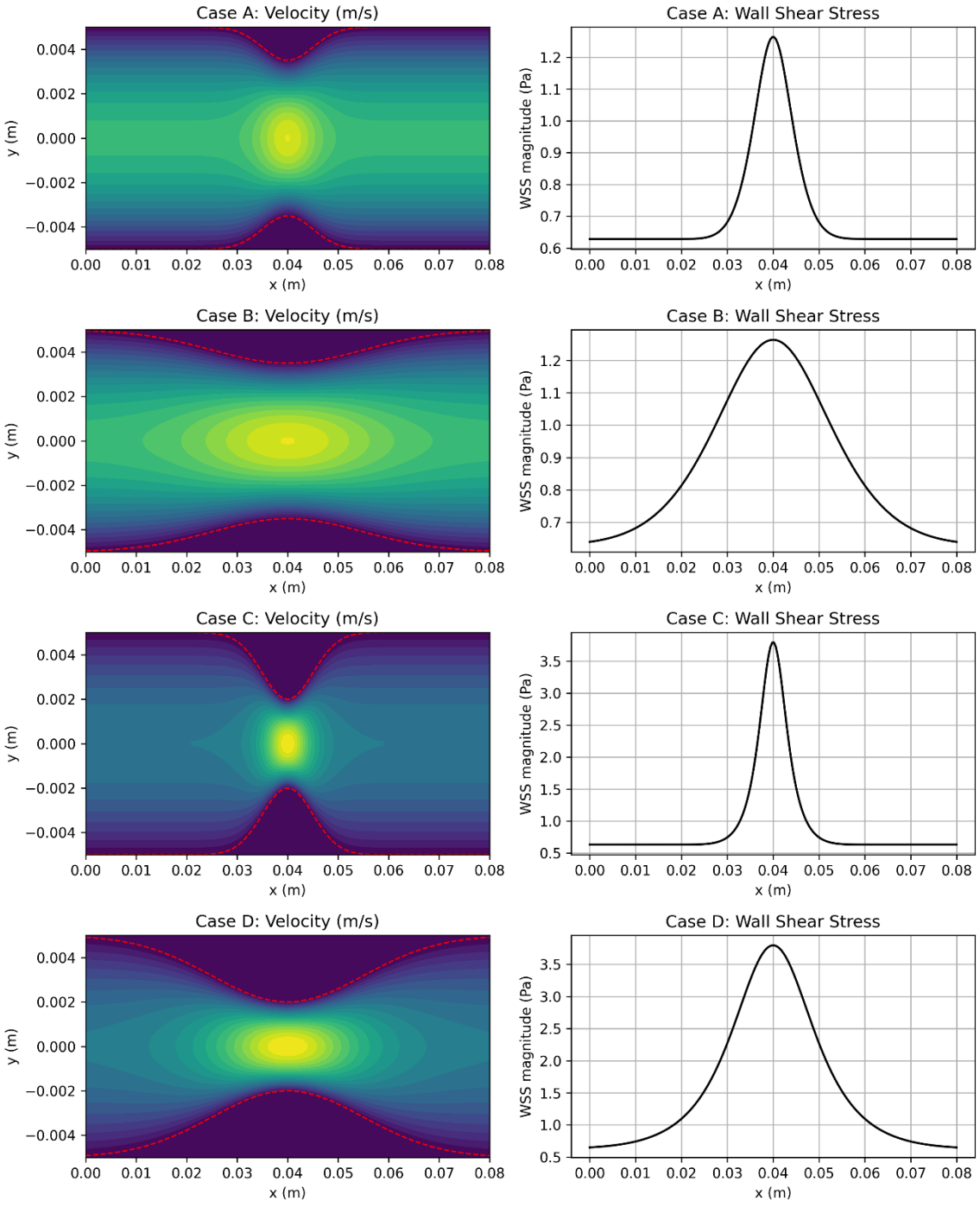

Figure 4. Velocity field (left) and wall shear stress magnitude (right) for the four stenosis configurations (Cases A–D).

Across the sampling grids, all three objectives increased as δ, μ0, and n increased and decreased as λ increased at every grid point. As σ increased, ΔP and Φ increased, whereas WSS_max did not change with σ, as presented in **Table 3**. The non-dominated subset of each grid contained a single point, located at the same corner as the NSGA-II outcome. The Pearson correlations between each parameter and each objective were as follows: for δ, +0.93, +0.77 and +0.77 with WSS_max, ΔP, and Φ, respectively; for σ, −0.01, +0.43 and +0.43; for μ0, +0.39, +0.42 and +0.43; for n, +0.71 with each objective; and for λ, from −0.07 to −0.09.

Table 3. Outcome of the two NSGA-II searches and of the exhaustive grid evaluation (reduced-order model).

Search	Bounds	Corner returned (NSGA-II and grid)	WSS_max (Pa)/ΔP (Pa) /Φ (W/m) at corner	Direction of change, other parameters fixed	Pearson r (WSS_max, ΔP, Φ)
Geometry (rheology at baseline)	δ ∈ [0.20, 0.70]; σ ∈ [0.003, 0.020] m	δ=0.20; σ=0.003 m	0.97/10.8/ 0.029	All three increase with δ; ΔP and Φ increase with σ; WSS_max independent of σ	δ: +0.93, +0.77, +0.77; σ: −0.01, +0.43, +0.43
Rheology (geometry of Case C)	μ0 ∈ [0.005, 0.056] Pa·s; n ∈ [0.3568, 0.80]; λ ∈ [3.313, 39.418] s	μ0=0.005 Pa·s; n=0.3568; λ=39.418 s	3.50/20.2/ 0.054	All three increase with μ0 and n and decrease with λ	μ0: +0.39, +0.42, +0.43; n: +0.71, +0.71, +0.71; λ: −0.07, −0.08, −0.09

NSGA-II: non-dominated sorting genetic algorithm II; WSS_max: maximum wall shear stress; ΔP: pressure drop; Φ: viscous energy dissipation rate per unit depth; δ: maximum degree of stenosis; σ: Gaussian width parameter; μ0: zero-shear viscosity; n: shear-thinning index; λ: Carreau–Yasuda time constant; r: Pearson correlation coefficient

Transient three-dimensional COMSOL simulation

The velocity magnitude in the stenosed pulmonary-artery model at t=2.4 s is presented in **Figure 5A**. The cross-sections in the proximal trunk showed the lowest velocity magnitudes, and those in the distal branches showed the highest.

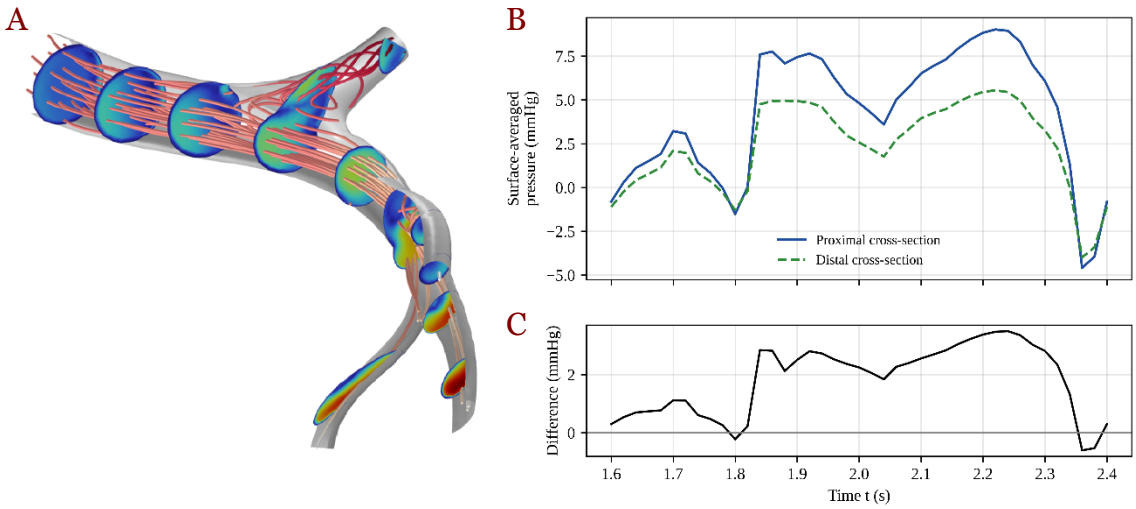

Figure 5. Transient COMSOL simulation of the stenosed pulmonary artery. (A) Velocity magnitude on cross-sections at t=2.4 s (color scale from blue, low, to red, high); (B) surface-averaged pressure on the proximal and distal cross-sections of the stenosis over t=1.6–2.4 s; and (C) their difference. Pressures are gauge values in mmHg relative to the zero-pressure outlets.

The proximal and distal pressures over t=1.6–2.4 s are presented in **Figure 5B** and **5C**. Proximal pressure exceeded distal pressure at most time points. The difference averaged 1.8 mmHg and peaked at 3.5 mmHg at t=2.24 s. It was negative at t=1.80 s (−0.2 mmHg) and at t=2.36–2.38 s (minimum −0.6 mmHg at t=2.36 s). The proximal pressure ranged from −4.6 mmHg at t=2.36 s to 9.0 mmHg at t=2.22 s.

Discussion

The results address the three gaps set out in the Introduction, within the limits of the reduced-order model. The first concerns geometry itself: by treating stenosis severity (δ) and width (σ) as continuously tunable parameters rather than fixed idealized shapes, this study shows that geometry alone, independent of any change in fluid rheology, can move throat WSS from within the healthy range to well above it. Case C (δ=0.6, σ=0.005) produced peak velocities and WSS gradients markedly higher than Case B (δ=0.3, σ=0.015), despite both cases sharing identical

blood properties. This is consistent with computational and imaging-based observations that abnormal shear forces correlate with endothelial dysfunction and atherogenic risk [4,6,7], but extends these observations by showing the same relationship emerging from a controllable, optimizable geometric model rather than a single fixed patient geometry, although lower WSS in this model does not by itself mean lower vascular risk. Peak velocity and maximum WSS depended only on δ because both are evaluated at the throat radius $R_0(1 - \delta)$, whereas a wider stenosis keeps the lumen narrow over a longer segment, thereby increasing the integrated pressure drop and energy loss. At δ=0.3, the throat WSS (1.26 Pa) was within the ~1.0–1.5 Pa typical of healthy arterial segments, whereas at δ=0.6 (3.80 Pa), it exceeded that range. High WSS at a stenosis throat has been associated with endothelial damage and plaque vulnerability, and low or oscillatory WSS downstream with atherogenic behavior [1,7]; the present steady, prescribed-profile model resolves neither recirculation nor oscillatory shear. The geometric search corner had a maximum WSS of 0.97 Pa, slightly below the lower end of the 1–7 Pa reporting range, highlighting that minimizing the selected outputs does not steer the solution toward a physiological range.

The second gap concerns rheology. Placing the Carreau–Yasuda parameters (μ_0, n, λ) in a search of their own, separate from the geometric search, treats rheology as a variable rather than as the fixed input used in prior forward studies [5,6,9,11]. Blood rheology is a patient-specific characteristic rather than a design choice: hematocrit, plasma proteins, and disease state all shift μ_0 and n. The rheological search is therefore best read as a sensitivity analysis of how the selected outputs respond across a range of rheological profiles, not as a search for a rheology to be selected. In the present formulation, rheology does not alter the velocity field, so geometry and rheology each move WSS, pressure drop, and energy loss in the same direction within their own search. Because the two searches were run separately, the study does not test whether a change in rheology could offset a change in geometry, and it makes no claim about such compensation.

These searches would be of limited use if they were directed at the wrong objective, which brings the discussion to the third gap: what is being optimized, not just how. Pareto-based CFD optimization has previously targeted implanted devices almost exclusively, including stent geometry [32,33] and the hemolytic performance of an artificial heart pump [30], all evaluating the performance of a manufactured object [40]. The closest precedent applied topology optimization to a coronary stent while considering hemodynamic parameters [34], but the object of optimization remained the stent, not the native diseased vessel. This study instead explores the stenosis profile itself, and separately the blood rheology that flows through it, against WSS, pressure drop, and energy loss, a formulation aimed at the arterial pathology rather than a downstream device. Stent-design optimization tells a manufacturer how to build a better stent. Stenosis-profile analysis of the kind explored here asks which post-intervention geometries lower hemodynamic load, and it could address that question once validated on patient-specific geometry.

The three gaps were addressed under a steady-state assumption. The separate COMSOL simulation in the present study is illustrative only: it shares neither geometry nor rheology with the reduced-order model and reports pressure rather than WSS. Proximal pressure exceeded distal pressure for most of the cycle, consistent with the added resistance of the narrowed segment, and the brief reversals at t=1.80 s and t=2.36–2.38 s coincided with rapid flow deceleration, when fluid inertia rather than viscous resistance sets the pressure difference. This time-dependent pressure behavior is consistent with that reported in a data-assimilation study of aortic flow [16]. It does not show that steady WSS understates systolic risk, but it indicates that time-dependent indices would be a natural target for future optimization studies, which so far rely on steady values, as do earlier device studies [32-34] and the present work.

The single corner reflects the prescribed kinematics: geometry alone determines the velocity and shear-rate fields, while rheological parameters affect viscosity without altering those fields. Consequently, each objective changes monotonically with the varied parameters within its respective search (Methods). The evolutionary searches therefore add little that the derivation does not already give: the analytical argument identifies the boundary optima directly, and NSGA-II recovers the same corners. Their contribution is computational. They show how a standard Pareto-based search behaves when the objectives are aligned, with the first front

contracting onto one boundary point instead of spreading, and they provide a search harness that can be reused unchanged with a formulation whose objectives might compete. They do not reveal competing optimal solutions, and the corners they return are not clinically actionable configurations, since each corner reflects the chosen objectives and bounds. The absence of a spread Pareto front within this formulation and these domains is the main methodological finding of the study.

From a clinical perspective, high-WSS zones and disturbed recirculation patterns are established markers of vascular injury and atherogenic risk in the wider literature [1,7]. However, the reduced-order model used in this study, which employs a prescribed steady parabolic profile, does not itself resolve recirculation (see Methods). The elevated energy loss in this study's results signals reduced perfusion efficiency downstream of the stenosis. Because the search operates directly on the geometric parameters (δ, σ) that describe a stenosis, the four representative configurations (rather than a spread Pareto-optimal set, given the structural finding above) can still be mapped onto clinically measurable quantities, such as percentage diameter reduction and lesion length. Any clinical use of that mapping would first require validation against patient-specific imaging and measured pressure gradients; the present model supplies no threshold for residual stenosis, device sizing, or intervention timing.

Three limitations qualify the framework's present readiness. First, the model itself is a reduced-order, lubrication-theory formulation (a locally prescribed parabolic velocity profile satisfying mass conservation at each axial position), rather than a fully iterative finite-volume Navier–Stokes solve; it also uses one cross-sectional viscosity, evaluated at the wall shear rate, in the pressure-gradient relation, and it assumes rigid walls and a symmetric planar geometry, neglecting fluid–structure interaction and any asymmetric plaque morphology, while separately, the Carreau–Yasuda rheology captures shear-thinning but not the non-linear viscoelastic character of blood itself explored in other vascular contexts [21]. Because the velocity field in this formulation is prescribed from the geometry and does not respond to local viscosity, the three objectives change monotonically with each parameter (see Results), and no spread Pareto front arises within the stated domains. The formulation also neglects convective inertia, although the inlet Reynolds number is about 720, and it cannot represent flow separation or recirculation near the throat. Second, the optimization was demonstrated for steady-state conditions, with pulsatility appearing only in the separate, unmatched COMSOL simulation; a fully coupled pulsatile-optimization loop has not yet been implemented. Third, the four representative cases and the physiological bounds on $(\mu_0, n, \lambda, \delta, \sigma)$ were set from literature values rather than patient-specific measurements, so the configurations reported here should be read as a proof of concept for the framework rather than a patient-ready prescription.

Four extensions follow from these limitations. First, a fully coupled momentum–viscosity formulation, such as a finite-volume Navier–Stokes implementation of the governing equations in Methods, would allow the velocity field to respond to local viscosity. Whether this coupling, compliant walls, or viscoelastic rheology would produce competing objectives remains an open question that requires investigation. The limitation associated with steady-state modeling points to replacing the steady-state objective functions with their time-integrated or peak-systolic equivalents, derived using a transient solver, so that the objectives capture time-dependent behavior. The geometric idealization gap could be addressed by extending the model from an idealized 2D Gaussian stenosis to patient-specific 3D reconstructions obtained from CT or IVUS imaging, in the spirit of [4,41], while retaining the multi-objective optimization structure.

Finally, adopting a fully coupled finite-volume solve would introduce substantial computational costs within an optimization loop, motivating the use of a faster reduced-order or surrogate model (e.g., Kriging or neural-network surrogates, as used for stent design [33]). Such a model could be trained on full-order simulation outputs, repurposing the type of approximation currently used in this study for computational tractability, but replacing the locally prescribed profile with a data-driven representation of the coupled flow solution. This approach could enable near-real-time, patient-specific "digital twin" feedback during interventional planning, which represents a long-term goal of this work. Pursuing these four directions in sequence would move the framework from a geometry- and rheology-search proof of concept toward a tool that could eventually be evaluated as a potential clinical decision-support system.

Conclusion

This study examined stenosis geometry and blood rheology as search variables in a reduced-order, lubrication-theory model of non-Newtonian flow through a Gaussian stenosis, using two separate NSGA-II searches over peak WSS, pressure drop, and viscous energy loss. Peak velocity and maximum WSS depended on stenosis severity alone, whereas pressure drop and energy loss also increased with stenosis width, and the severe, wide configuration (δ=0.6, σ=0.015 m) produced the largest integrated losses. Both searches converged to a single corner of their respective parameter domains, and an analytical argument, confirmed on sampling grids, showed that each objective changes in a fixed direction with each parameter, so the formulation yields no Pareto trade-off within these domains. The searches therefore demonstrate the structural behavior of this formulation rather than competing or clinically actionable optima, and the results should be read as a methodological proof of concept. A fully coupled momentum–viscosity solve, transient objectives, and patient-specific geometry remain important developments whose effects on the emergence of Pareto trade-offs require further investigation.

Ethics approval

Not required.

Acknowledgments

None to declare.

Competing interests

All the authors declare that there are no conflicts of interest.

Funding

This research was funded by Universitas Sumatera Utara through the International Collaboration Research scheme (Grant No: 36/UN5.4.10.K/PT.01.03/TALENTA/RB1/2025).

Underlying data

The Python scripts that implement the reduced-order model, the NSGA-II searches, the exhaustive grid evaluation and the figures, together with the COMSOL pressure time series presented in **Figure 5**, are openly available in Figshare at https://doi.org/10.17632/g6r4vw84rf.1 under a CC BY 4.0 license.

Declaration of artificial intelligence use

This study used artificial intelligence (AI) tools in the following capacity: manuscript writing support: an AI-based language model (Claude, Anthropic) was used for language refinement, including improving grammar, sentence structure, and readability. During revision, the same tool also assisted in re-implementing and checking the Python scripts for the reduced-order model, the NSGA-II searches and the figures; the authors verified all code, computed values and interpretations. We confirm that all AI-assisted processes were critically reviewed by the authors to ensure the integrity and reliability of the results. The final decisions and interpretations presented in this article were solely made by the authors.

How to cite

Tulus T, Marpaung JL, Aziz NA, *et al*. Parametric fluid mechanics study of vessel geometry and blood rheology: Structural absence of a Pareto trade-off. Narra X 2026; 4 (3): e353 - http://doi.org/10.52225/narrax.v4i3.353.

References

1. Katritsis DG, Theodorakakos A, Pantos I. Vortex formation and recirculation zones in left anterior descending artery stenoses: Computational fluid dynamics analysis. Phys Med Biol 2010;55(5):1395-1411.

2. Beier S, Ormiston J, Webster M. Hemodynamics in idealized stented coronary arteries: Important stent design considerations. Ann Biomed Eng 2016;44(2):315-329.
3. Wei L, Leo HL, Chen Q, *et al.* Structural and hemodynamic analyses of different stent structures in curved and stenotic coronary artery. Front Bioeng Biotechnol 2019;7:1-13.
4. Kamada H, Nakamura M, Ota H, *et al.* Blood flow analysis with computational fluid dynamics and 4D-flow MRI for vascular diseases. J Cardiol 2022;80(5):386-396.
5. Hamidah MA, Hossain SMC. Modeling analysis of pulsatile non-Newtonian blood flow in a renal bifurcated artery with stenosis. Int J Thermofluids 2024;22:100645.
6. Bashar MS, Hossain R, Rahman MH. CFD analysis of non-Newtonian blood flow through human carotid artery bifurcation: Carotid sinus susceptible to atherosclerosis. Heliyon 2024;10(22):e40286.
7. Liu H, Lan L, Abrigo J. Comparison of Newtonian and non-Newtonian fluid models in blood flow simulation in patients with intracranial arterial stenosis. Front Physiol 2021;12:1-11.
8. Pontrelli G. Blood flow through an axisymmetric stenosis. Proc Inst Mech Eng H 2001;215(1):1-10.
9. Almutairi S. Numerical way out through finite volume method for Navier-Stokes type blood flow inside stenosed curved arteries. J Eng Appl Sci 2024;11(1):63.
10. Ghasemiasl R, Ostadhossein R, Javadi MA, *et al.* Blood flow simulation in an aorta with a mild coarctation using magnetic resonance angiography and finite volume method. Int J Eng 2018;31(4):673-678.
11. Sharma M, Sharma BK, Khanduri U. Optimization of heat transfer nanofluid blood flow through a stenosed artery in the presence of Hall effect and hematocrit dependent viscosity. Case Stud Therm Eng 2023;47:103075.
12. Khaliq S, Younas M, Abbas Z. Thermally radiative flow of non-Newtonian Rabinowitsch fluid through a permeable artery with multiple stenoses of varying shapes. J Radiat Res Appl Sci 2025;18(2):101400.
13. Adel M, Assiri TA, Khader MM. Numerical simulation by using the spectral collocation optimization method associated with Vieta-Lucas polynomials for a fractional model of non-Newtonian fluid. Results Phys 2022;41:105927.
14. Bhatnagar A, Shrivastav RK, Singh AK. A numerical analysis for the effect of slip velocity and stenosis shape on non-Newtonian flow of blood. Int J Eng 2015;28(3):440-446.
15. Udupa MC, Saha S, Natarajan S. Study of blood flow patterns in a stenosed artery through the combined effect of body acceleration and generalized Womersley solution. Sci Rep 2025;15(1):1845.
16. Anwar MA, Tiago J. Time-dependent strategy for improving aortic blood flow simulations with boundary control and data assimilation. Appl Math Comput 2025;493:129266.
17. Samal S, Ontela S. Sensitivity analysis and optimization of heat transfer in the time-reliant magnetohydrodynamic bioconvective flow of radiative couple-stress hybrid nanofluid through a squeezing channel with viscous dissipation: Entropy analysis. Hybrid Adv 2024;7:100258.
18. Singh AK, Singh DP. MHD flow of blood through radially non-symmetric stenosed artery: A Herschel-Bulkley model. Int J Eng 2013;26(8):859-864.
19. Gupta AK. Performance model and analysis of blood flow in small vessels with magnetic effects. IJE Trans Basics 2012;25(7):189-196.
20. Pontrelli G. Blood flow through a circular pipe with an impulsive pressure gradient. Math Models Methods Appl Sci 2000;10(2):187-202.
21. Pinto SIS, Romano E, Conceição António CA. The impact of non-linear viscoelastic property of blood in right coronary arteries hemodynamics: A numerical implementation. Int J Non Linear Mech 2020;123:103477.
22. Yadav N, Jaiswal S, Yadav PK. Two-phase magnetohydrodynamic blood flow through curved porous artery. Phys Fluids 2024;36(9):091924.
23. Rehman S, Alqahtani S, Eldin SM, *et al.* An extended model to assess Jeffery-Hamel blood flow through arteries with iron-oxide (Fe2O3) nanoparticles and melting effects: Entropy optimization analysis. Nanotechnol Rev 2024;13(1):1-20.
24. Jeffrey ASA, Shanmugapriya M, Sundareswaran R. Casson ternary hybrid nanofluid blood flow through bell, symmetrical and trapezoidal shaped constricted inclined arteries: Implications for targeted drug delivery. Chin J Phys 2026;103:476-516.
25. Dawood AS, Kroush FA, Abumandour RM, *et al.* Comparative analysis of pulsatile nanofluid flow under slip conditions through stenosed arteries. Bound Value Probl 2025;2025:28.
26. Oh J-T, Chien NB. Optimization design by coupling computational fluid dynamics and genetic algorithm. In: Lonescu A, editor. Computational fluid dynamics - basic instruments and applications in science. IntechOpen; 2018.

27. Kumar P, K G V, Almeida F, *et al.* Optimization using response surface methodology for Eyring-Powell fluid flow with Cattaneo-Christov heat flux and cross diffusion effects. Int J Thermofluids 2025;25:100981.
28. Diallo AB, Yapici R, Incebay O, *et al.* Geometric optimization of a blood pump impeller using the Taguchi method: CFD analysis and experimental evaluation. Med Nov Technol Devices 2025;26:100364.
29. Gu K, Yang K, Zhao C, *et al.* Optimizing the design of a pediatric blood pump through orthogonal experimentation. Heliyon 2025;11(4):e42502.
30. Liu X, Huang C, Sheng Y. Optimization of hemolytic performance of artificial heart pump based on CFD. Heliyon 2025;11(4):e42635.
31. Russ JB, Li RL, Herschman AR. Design optimization of a cardiovascular stent with application to a balloon expandable prosthetic heart valve. Mater Des 2021;209:109977.
32. Gundert TJ, Marsden AL, Yang W, *et al.* Optimization of cardiovascular stent design using computational fluid dynamics. J Biomech Eng 2012;134(1):011002.
33. Li H, Gu J, Wang M. Multi-objective optimization of coronary stent using Kriging surrogate model. Biomed Eng Online 2016;15(s2):275-291.
34. Ahadi F, Azadi M, Biglari M, *et al.* Topology optimization of coronary artery stent considering structural and hemodynamic parameters. Heliyon 2024;10(20):e39452.
35. Salman HE, Yalcin HC. Computational modeling of blood flow hemodynamics for biomechanical investigation of cardiac development and disease. J Cardiovasc Dev Dis 2021;8(2):1-27.
36. Tulus, Rasani MR, Rahman M. Biomedical simulation of non-Newtonian fluid dynamics in cardiovascular systems: A finite volume method approach to pulsatile flow and atherosclerosis analysis. Int J Energy Prod Manag 2024;9(4):275-285.
37. Ahmed H, Podder C. Hemodynamical behavior analysis of anemic, diabetic, and healthy blood flow in the carotid artery. Heliyon 2024;10(4):e26622.
38. Deb K, Pratap A, Agarwal S, *et al.* A fast and elitist multiobjective genetic algorithm: NSGA-II. IEEE Trans Evol Comput 2002;6(2):182-197.
39. COMSOL AB. Blood flow in a stenosed pulmonary artery (Application ID 131371), 2024.
40. Ali SM. A novel design and simulation of a nano prosthetic artificial heart valve. Int J Eng 2024;37(02):237-251.
41. Batteux C, Abakka S, Gaudin R. Three-dimensional geometry of coronary arteries after arterial switch operation for transposition of the great arteries and late coronary events. J Thorac Cardiovasc Surg 2021;161(4):1396-1404.